

# Quadratic Time–Frequency Analysis of Vibration Signals for Diagnosing Bearing Faults

Mohammad Al-Sa'd, *Senior Member, IEEE*, Tuomas Jalonen, Serkan Kiranyaz, *Senior Member, IEEE*, and Moncef Gabbouj, *Fellow, IEEE*

**Abstract**—Diagnosis of bearing faults is paramount to reducing maintenance costs and operational breakdowns. Bearing faults are primary contributors to machine vibrations, and analyzing their signal morphology offers insights into their health status. Unfortunately, existing approaches are optimized for controlled environments, neglecting realistic conditions such as time-varying rotational speeds and the vibration's non-stationary nature. This paper presents a fusion of time-frequency analysis and deep learning techniques to diagnose bearing faults under time-varying speeds and varying noise levels. First, we formulate the bearing fault-induced vibrations and discuss the link between their non-stationarity and the bearing's inherent and operational parameters. We also elucidate quadratic time-frequency distributions and validate their effectiveness in resolving distinctive dynamic patterns associated with different bearing faults. Based on this, we design a time-frequency convolutional neural network (TF-CNN) to diagnose various faults in rolling-element bearings. Our experimental findings undeniably demonstrate the superior performance of TF-CNN in comparison to recently developed techniques. They also assert its versatility in capturing fault-relevant non-stationary features that couple with speed changes and show its exceptional resilience to noise, consistently surpassing competing methods across various signal-to-noise ratios and performance metrics. Altogether, the TF-CNN achieves substantial accuracy improvements up to 15%, in severe noise conditions.

**Index Terms**—Bearing fault, damage detection, deep learning, time-frequency analysis, variable speed.

## I. INTRODUCTION

ROTATING machinery, such as motors, gearboxes, wind turbines, generators, and engines, is at the heart of modern industrial applications [1]. Condition monitoring and fault diagnosis of rotating machinery allow proactive maintenance strategies and reduce economic and operational impacts caused by unexpected failures [2]. Bearing faults constitute a prominent category of irregularities in rotating machines; thus, continuous monitoring is imperative [2], [3]. Fortunately, abnormal machine vibrations are largely a result of faulty bearings, and analyzing their characteristics facilitates diagnosing the bearing's health condition [4], [5], [6], [7].

This work was supported by Business Finland Amalia and NSF IUCRC CBL project. (*Corresponding author: Mohammad Al-Sa'd.*)

Mohammad Al-Sa'd is with the Faculty of Medicine, University of Helsinki, 00014 Helsinki, Finland (e-mail: mohammad.al-sad@helsinki.fi) and the Faculty of Information Technology and Communication Sciences, Tampere University, 33720 Tampere, Finland mohammad.al-sad@tuni.fi).

Tuomas Jalonen and Moncef Gabbouj are with the Faculty of Information Technology and Communication Sciences, Tampere University, 33720 Tampere, Finland (e-mail: tuomas.jalonen@tuni.fi; moncef.gabbouj@tuni.fi).

Serkan Kiranyaz is with the Department of Electrical Engineering, Qatar University, 2713 Doha, Qatar (e-mail: mkiranyaz@qu.edu.qa).

Deep learning techniques, such as Convolutional Neural Networks (CNNs), are adequate to diagnose the bearing's condition by detecting irregularities in the vibration data [8], [9], [10], [11]. Nevertheless, prevailing solutions are usually tested under ideal conditions and often confined to fixed [12], [13], [14] or slowly increasing/decreasing rotational speeds [15], [16] that do not represent dynamic scenarios [4], i.e., time-varying changes. The vibratory profile of bearings under time-varying rotational speeds is strictly non-stationary [17], i.e., vibration is modulated by speed and characterized by a time-varying spectral content [18], [19]. Therefore, classical time- or frequency-domain representations are insufficient, and one must adopt time-frequency (TF) tools to explore the signal's degrees of freedom [20]. Therefore, in this paper, we propose to leverage synergies between TF analysis and deep learning to diagnose bearing faults under highly time-varying rotational speeds. The key contributions of this paper are:

- Quadratic time-frequency distributions are effective for revealing distinctive dynamic patterns that are associated with different bearing faults.
- A bearing fault diagnosis system fusing quadratic time-frequency distributions and CNNs with robustness to diverse noise levels and time-varying speed conditions.
- Precise identification of various bearing faults with performance significantly surpassing recently developed techniques about 15% gain in average accuracy.

Time-frequency representations (TFR) fall under two complementary categories; linear and quadratic [18]. Linear TFRs, such as short-time Fourier transform and continuous wavelet transform, extend the signal's spectrum to become time-dependent [18]. Specifically, they use a set of basis functions for decomposition and yield time-varying complex-valued frequency representations [21]. The resolution of linear TFRs is limited by the Heisenberg-Gabor uncertainty principle [21], [22]. However, quadratic TFRs, derived from the Wigner-Ville distribution (WVD), overcome this limitation by transforming the signal's time-varying auto-correlation function [18]. Nevertheless, this advantage is at the expense of reducing accuracy by introducing artifactual patterns, named cross-terms, that require filtering [23]. Fortunately, high-performing distributions are designed to achieve the best trade-off between accuracy and resolution [23].

The utility of linear TFRs was found useful for analyzing various faults in rolling-element bearings [24], [25], [26] and for classifying their health states [27], [28], [29]. Nonetheless, most experiments were conducted with limited speed profiles

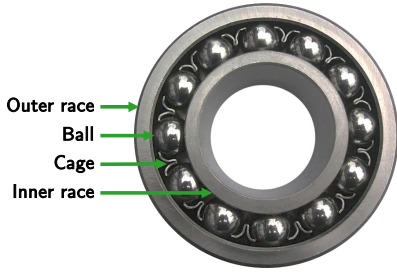


Fig. 1. A rolling element bearing example. The bearing's outer race, inner race, balls, and cage are illustrated. Redrawn from [39].

and were confined to constant [29], [30], fixed levels [28], or slowly varying speeds with limited range [31]. Besides, some studies focused on analyzing the extracted features rather than reporting validated classification results [24], [26], [32]. Moreover, quadratic TFRs were utilized in only a few studies using elementary distributions [33], [34], [35], although there are better high-performing alternatives such as the compact kernel distribution, smoothed-pseudo Wigner-Ville distribution, and the extended modified B-distribution [23]. In fact, a recent review reveals that the literature is dominantly focused on developing post-processing techniques for quadratic TFRs rather than utilizing more advanced representations [36]. Consequently, there is a need for fusing high-performing quadratic TFRs with deep learning techniques to build a precise tool for diagnosing non-stationary bearing faults.

## II. METHODOLOGY

The role of a ball bearing is to reduce friction and to provide support for both radial and axial loads [37]. This is achieved by enclosing the steel rollers with two races to enable load transmissions [37]; see Fig. 1. Fatigue in bearings introduces spalling, a common type of damage that primarily occurs on the races and the rolling elements, and changes the machine's vibratory profile [38]. Under time-varying rotational speeds, this fault-induced alteration becomes dynamic and co-varies with the motor's speed. In other words, speed modulates the vibrations and makes them non-stationary, i.e., characterized by time-varying spectra. Therefore, we combined TF analysis and deep learning techniques to develop a precise tool for diagnosing non-stationary faults in bearings.

### A. Signal model

The bearing vibrations, captured by accelerometers mounted on the horizontal and vertical axes of the bearing's housing, can be generally modeled by:

$$\mathbf{x}(t) = \mathbf{s}(t) + \alpha \boldsymbol{\eta}(t), \quad (1)$$

where  $\mathbf{x}(t) = [x_x(t), x_y(t)]^T$  holds noisy vibrations recorded by the accelerometers mounted on the x and y directions,  $\mathbf{s}(t) = [s_x(t), s_y(t)]^T$  contains the bearing's noise-free vibrations in both directions,  $\boldsymbol{\eta}(t) = [\eta_x(t), \eta_y(t)]^T$  holds independent and identically distributed white Gaussian noise signals with zero mean and unit variance, and  $\alpha = [\alpha_x, \alpha_y]^T$  are factors that control the amount of noise-induced degradation

based on a predefined signal-to-noise ratio (SNR) in decibels (dB) and are calculated as follows:

$$\alpha = \sqrt{10^{-\text{SNR}/10} \frac{1}{T} \int_0^T \mathbf{s}^2(t) dt}, \quad (2)$$

where  $T$  is the time duration of the signals in  $\mathbf{s}(t)$ . The bearing noise-free vibrations are comprised of healthy patterns (random or deterministic) and fault-induced amplitude-modulated oscillations [40], [41], [42], i.e.:

$$\mathbf{s}(t) = \mathbf{h}(t) + \mathbf{f}(t), \quad (3)$$

$$\mathbf{f}(t) = \underbrace{A \sin(2\pi f_c t)}_{\text{Amplitude modulation}} \sum_{k=0}^K \underbrace{\left( e^{-\beta f_c t} \right)}_{\text{Fault impulses}} \underset{\text{Pulse frequency modulation}}{*} \delta \left( t - \frac{k}{f_{\text{fault}}(t)} \right), \quad (4)$$

where  $\mathbf{h}(t)$  holds the bearing normal vibration (healthy patterns),  $\mathbf{f}(t)$  is the fault-specific waveform,  $A$  is the fault amplitude,  $f_c$  is the bearing resonance frequency,  $\beta$  is the damping characteristic factor,  $*$  denotes convolution in time,  $\delta(t)$  is the Dirac function,  $f_{\text{fault}}(t)$  denotes the time-varying fault characteristic frequency, and  $K$  is the number of fault impulses, or knocks, within the signal duration  $T$ . The characteristic frequencies that appear in the vibration signal of a faulty bearing, assuming a stationary outer race and a rotating inner race, are mainly the ball pass frequency of the inner race, ball pass frequency of the outer race, and ball spinning frequency, which are expressed by [43]:

$$f_{\text{fault}}^{(\text{Inner})}(t) = \frac{n}{2} \left( 1 + \frac{D_r}{D_p} \cos(\theta) \right) f_r(t), \quad (5)$$

$$f_{\text{fault}}^{(\text{Outer})}(t) = \frac{n}{2} \left( 1 - \frac{D_r}{D_p} \cos(\theta) \right) f_r(t), \quad (6)$$

$$f_{\text{fault}}^{(\text{Ball})}(t) = \frac{D_p}{D_r} \left( 1 - \left( \frac{D_r}{D_p} \cos(\theta) \right)^2 \right) f_r(t), \quad (7)$$

where  $n$  is the number of rolling elements,  $D_r$  is the rolling element diameter,  $D_p$  is the pitch diameter,  $\theta$  denotes the contact angle, i.e., the angle of load from the radial plane, and  $f_r(t)$  is the motor's time-varying rotational frequency, i.e., number of rotations per second (rpm/60).

The bearing fault vibrations, expressed in Eq. (4), are comprised of three parts: amplitude modulation (AM), fault-induced impulses, and pulse frequency modulation (PFM); see Figs. 2a-2c for an example. First, the PFM component encodes the fault time-varying frequency which, by examining Eqs. (5)-(7), depends on the bearing's geometry, the fault location, the motor's rotational speed, and the contact angle. Specifically, the bearing's geometry and the location of the fault are responsible for defining the fault's base harmonics, the motor's rotational speed shifts the base spectrum in a time-dependent manner, and variations in the contact angle due to misalignment, thermal growth, excessive bolt tightening, and pitting/peeling in the bearing races induce further frequency disruptions [44]. Moreover, the fault impulses in Eq. (4) express the rolling element rattlings that depend on the bearing geometry and emerge with the frequency defined by the PFM. Finally, the AM component carries the frequency-modulated

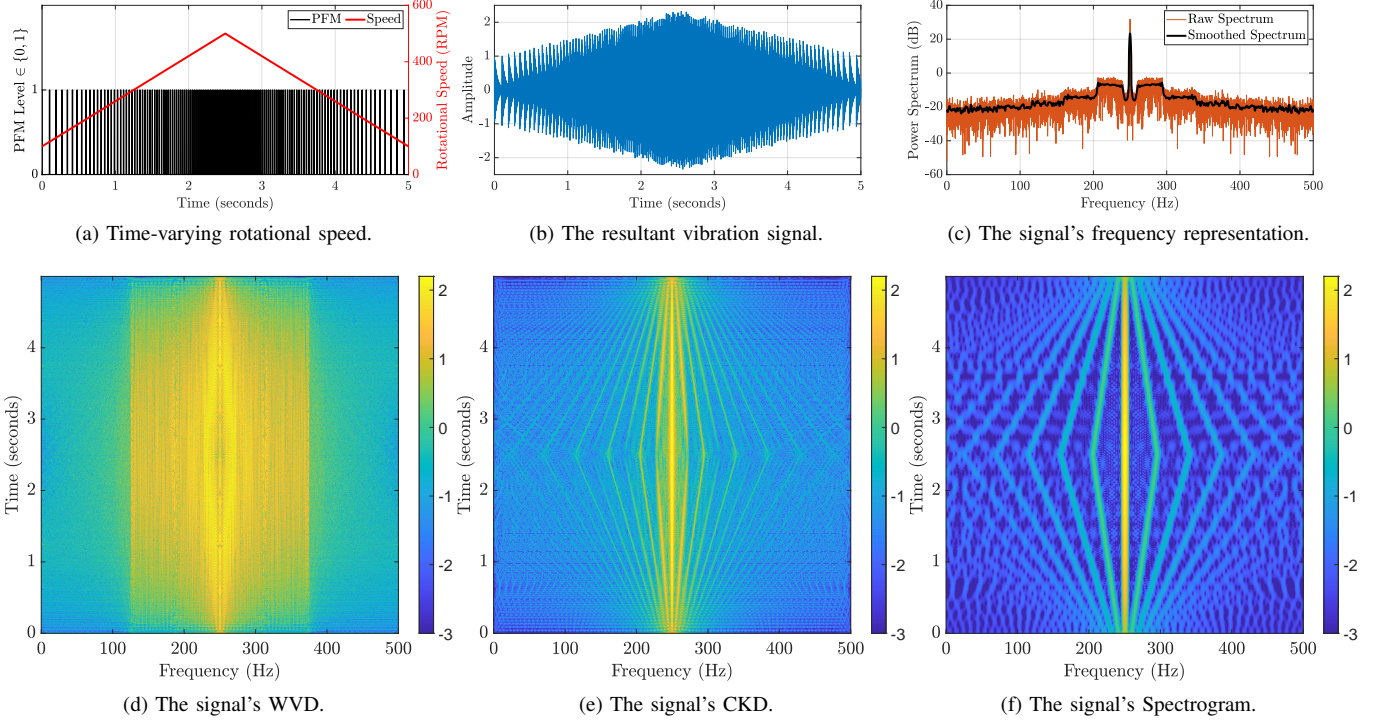


Fig. 2. Example synthetic bearing vibration signal with an inner race fault following Eq. (4). (a) shows the linearly changing rotational speed in red and its pulse frequency modulation (PFM) encoding in black, (b) depicts the generated vibration signal, (c) illustrates its power spectrum, and (d)-(f) show the compact kernel distribution (CKD) high accuracy, compared to the Wigner-Ville distribution (WVD), and its high resolution, compared to the Spectrogram, when representing the vibration signal in the time-frequency domain. The signal model parameters are set to  $f_s = 1$  kHz,  $T = 5$  seconds,  $A = 1$ ,  $f_c = 250$  Hz,  $\beta = 0.1$ ,  $n = 9$ ,  $D_r = 7.9$  mm,  $D_p = 38.5$  mm,  $\theta = 0^\circ$ , and  $f_r(t)$  is a triangular wave rising from 100 rpm to 500 rpm and back to 100 rpm. The CKD parameters are set to  $c = 1$ ,  $D = 0.1$ ,  $E = 0.1$ , and the Spectrogram is computed at full resolution using a 0.3 seconds Hamming window. The TFRs are plotted on a logarithmic scale to ease visualizing the fault-induced waveforms around the bearing's resonance at 250 Hz (-3 dB to 2.2 dB).

impulses to the bearing's resonance frequency. Altogether, the vibration signal of a faulty bearing, under time-varying rotational speed conditions, is strictly non-stationary and mandates TF tools for analysis and processing.

### B. Quadratic time-frequency representation

A time-frequency representation (TFR), obtained by a time-frequency distribution (TFD), describes the vibrations spectra through time [18], i.e., it reveals the vibrations' joint temporal and spectral evolution [23]. Let  $\mathbf{z}(t) = [z_x(t), z_y(t)]^T$  be the analytic associate of the vibration signals in  $\mathbf{x}(t)$  obtained via the Hilbert transform, such that:

$$\mathbf{z}(t) = \mathbf{x}(t) + j\mathcal{H}\{\mathbf{x}(t)\}, \quad (8)$$

where  $\mathcal{H}\{\cdot\}$  is the Hilbert transform and  $j = \sqrt{-1}$ . The Wigner-Ville distribution (WVD) of  $\mathbf{z}(t)$  is defined as [23]:

$$\mathbf{W}_z(t, f) = \mathcal{F}_{\tau \rightarrow f} \left\{ \mathbf{z} \left( t + \frac{\tau}{2} \right) \mathbf{z}^* \left( t - \frac{\tau}{2} \right) \right\}, \quad (9)$$

where  $\mathbf{W}_z(t, f)$  holds the WVDs of the signals in  $\mathbf{z}(t)$ ,  $\mathcal{F}_{\tau \rightarrow f}\{\cdot\}$  denotes the Fourier transform (FT) from lag  $\tau$  to frequency  $f$ , and  $\mathbf{z}^*(t)$  is the complex conjugate of  $\mathbf{z}(t)$  [45]. The WVD is optimal for mono-component linear frequency modulated signals, but when analyzing other signal types, it is known to suffer from interference patterns, named cross-terms,

because of its bilinear nature [23]. The cross-terms severity can be reduced by a TF smoothing kernel  $\gamma(t, f)$  such that:

$$\rho_z(t, f) = \gamma(t, f) \underset{(t, f)}{**} \mathbf{W}_z(t, f), \quad (10)$$

where  $\rho_z(t, f)$  holds smoothed TFDs and  $**_{(t, f)}$  denotes the convolution in time and frequency. This expression can be written in a more convenient space, called the Doppler-lag domain, where convolutions become multiplications [18], i.e.:

$$\rho_z(t, f) = \mathcal{F}_{t \leftarrow \nu}^{-1} \left\{ \mathcal{F}_{\tau \rightarrow f} \left\{ g(\nu, \tau) \mathbf{A}_z(\nu, \tau) \right\} \right\}, \quad (11)$$

$$g(\nu, \tau) = \mathcal{F}_{\tau \leftarrow f}^{-1} \left\{ \mathcal{F}_{t \rightarrow \nu} \left\{ \gamma(t, f) \right\} \right\}, \quad (12)$$

$$\mathbf{A}_z(\nu, \tau) = \mathcal{F}_{t \rightarrow \nu} \left\{ \mathbf{z} \left( t + \frac{\tau}{2} \right) \mathbf{z}^* \left( t - \frac{\tau}{2} \right) \right\}, \quad (13)$$

where  $\mathcal{F}_{t \leftarrow \nu}^{-1}\{\cdot\}$  denotes the inverse FT from Doppler  $\nu$  to time  $t$ ,  $g(\nu, \tau)$  is the Doppler-lag kernel, and  $\mathbf{A}_z(\nu, \tau)$  is the ambiguity function (AF). The Doppler-lag kernel's role is to mitigate the WVD cross-terms while concurrently preserving the resolution of its auto-terms, which encapsulate the genuine content [21]. Employing a compact kernel distribution (CKD) stands out as a highly effective method for accomplishing this critical task [23]. Besides, it is more suitable for resolving the vibration waveforms of faulty bearings in the TF domain

when compared to the WVD and Spectrogram; see Figs. 2d-2f. The CKD utilizes a separable compact support kernel that is comprised of two parts operating independently in the Doppler-lag domain such that:

$$g(\nu, \tau) = G(\nu) \mathcal{G}(\tau), \quad (14)$$

$$G(\nu) = \exp\left(c + \frac{cD^2}{\nu^2 - D^2}\right) : |\nu| < D, \quad (15)$$

$$\mathcal{G}(\tau) = \exp\left(c + \frac{cE^2}{\tau^2 - E^2}\right) : |\tau| < E, \quad (16)$$

where  $G(\nu)$  and  $\mathcal{G}(\tau)$  are the independent Doppler and lag kernels, respectively,  $D \in [0, 1]$  and  $E \in [0, 1]$  are the kernel normalized cut-offs along the Doppler and lag axes, respectively, and  $c > 0$  defines the shape of the kernel.

### C. Bearing fault diagnosis

1) *Dataset description*: This study utilizes an open-access dataset collected at the Korean Advanced Institute of Science and Technology (KAIST) [46]. The dataset focuses on diagnosing bearing faults under time-varying motor speeds. The conducted experiments include vibration signals captured at 25.6 kHz by accelerometers installed on the x- and y-axes of a bearing housing [46]. Faults were induced in the bearing, and vibration data was recorded for four distinct health states: *Normal*, *Outer*, *Inner*, and *Ball*, delineating a typical bearing function and three common faults. In total, 35 minutes of multi-sensor data was collected for each of the four classes.

2) *Data processing and representation*: The accelerometer waveforms were first downsampled to 20 kHz using a finite impulse response anti-aliasing lowpass filter with delay compensation, which resulted in 42M samples for each sensor and bearing state. After that, we divided the signals' temporal course into smaller segments with no overlap to prevent any unintended data leakage when training and/or testing the fault diagnosis system. However, selecting an appropriate segment length requires careful consideration. On one hand, it must be sufficiently small to provide an ample number of samples for training while minimizing additional complexities stemming from the motor's variable speed. On the other hand, it should be broad enough to encompass intricate patterns and capture class-specific features. We decided 0.1 seconds was suitable because the motor speed changes at a maximum rate of 10 Hz, as illustrated by the frequency analysis in Fig. 3. This segment length yields 21K segments for each sensor and bearing state. Moreover, we generated the TFR of each segment as follows: (1) form the signal's AF by Eq. (13); (2) multiply the AF with the compact support kernel ( $c = 1$ ,  $D = 0.1$ , and  $E = 0.1$ ) to suppress cross-terms; (3) revert the filtered AF to the TF domain using Eq. (11); (4) downsample the resultant TFR from  $2000 \times 2000$  to  $128 \times 128$  to reduce computational complexity (see Fig. 4 which demonstrates the CKD of an example segment for all the bearing health states); and (5) standardize the TFR to have zero mean and unit variance.

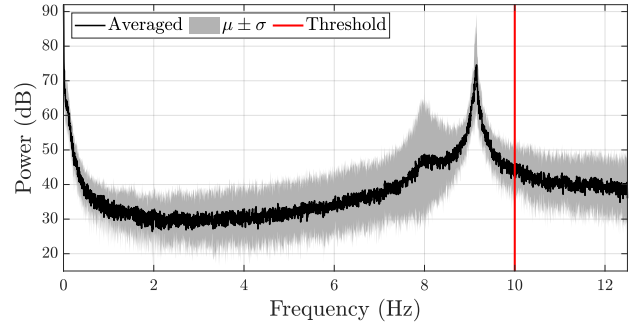


Fig. 3. Frequency analysis of the rotational speeds in the KAIST dataset. The motor speed exhibits variations at two distinct frequencies: 8 Hz and 9.15 Hz, with a maximum rate of change of 10 Hz as it includes 99.6% of the total power spectrum, covering nearly all rapid speed changes. The power spectrum is estimated by the nonuniform FT because of the speed's inconsistent acquisition rate, averaged across the classes and dataset files, and plotted along with its 68.3% confidence interval. Frequency scaling uses a 12.5 Hz sampling frequency which is the reciprocal of the shortest acquisition time.

3) *Time-frequency Convolutional Neural Network (TF-CNN)*: We developed a lightweight CNN architecture in a systematic manner, named TF-CNN, that accepts the standardized TFRs coming from both accelerometers (input size:  $128 \times 128 \times 2$ ). The input TFRs undergo processing through five convolutional blocks, each comprising a convolutional layer for feature extraction employing a ReLU activation function to address non-linear effects, and a max-pooling layer of size  $2 \times 2$  for summarizing the features. The convolutional layer in the first block has a kernel size of  $5 \times 5$ , while subsequent layers utilize kernels sized at  $3 \times 3$ . The features extracted from the final convolutional block are flattened and directed through a dense layer housing 128 nodes activated by ReLU. Subsequently, they traverse a dropout layer with 0.4 rate and a classification layer comprising 4 nodes with a Softmax activation function to transform the network's outputs to probabilities.

4) *Experiment settings*: We trained and tested the TF-CNN model in a 5-fold cross-validation fashion to accurately assess its capacity for generalization. Specifically, the 84K samples (four classes each containing 21K segments) were partitioned into five equally sized and shuffled stratified folds. Within this process, one fold served as the test set, while the remaining four were utilized for training. This procedure was iterated five times, and the training process extended across 150 epochs using an Adam optimizer to minimize categorical cross-entropy. We set the batch size to 100 and the learning rate to  $10^{-5}$  for epochs 0 to 100, followed by a reduced rate of  $10^{-6}$  for the rest of the epochs. Finally, we tested the model using the weights learned at the last epoch (no early stopping). In this study, we experimented with clean vibration signals and those degraded by noise at 5 dB, 0 dB, and -5 dB SNRs. Despite the varying noise levels, we utilized the same TF-CNN architecture and training configurations. Additionally, we compared the TF-CNN to two techniques recently developed for the KAIST dataset; PIResNet [47] and an efficient time-domain CNN (T-CNN) [4]. These comparisons are largely for testing the value of representing the vibration signals in the TF domain via quadratic TFDs.

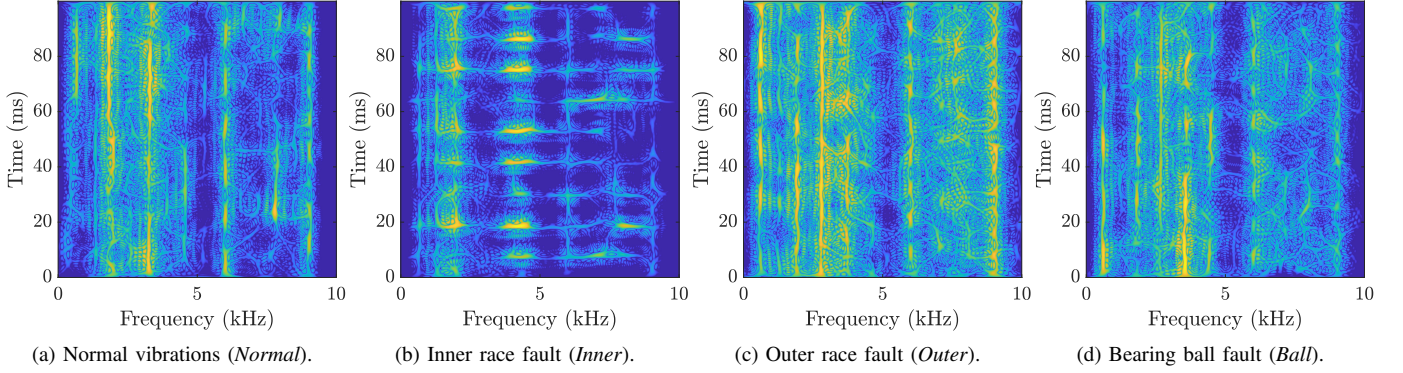


Fig. 4. The CKD of the first vibration segment from the sensor mounted on the y-direction with no noise. The representations’ magnitudes are plotted on a logarithmic scale to ease visualization (-3 dB to 0 dB).

5) *Performance evaluation and analysis*: We evaluated the diagnosis of multiple bearing faults in a one-versus-all fashion, converting the original multi-class problem into a series of binary classification tasks. We quantified the models’ efficacy in each task by accuracy, precision, recall, and F1-score, and then averaged these measures across all tasks. Moreover, the TF-CNN was assessed using t-distributed stochastic neighbor embedding (t-SNE) and Gradient-weighted Class Activation Mapping (Grad-CAM) to allow an understanding of its predictions when presented with new vibration signals. Specifically, t-SNE reduces data dimensionality by grouping similar samples and separating dissimilar ones [48], and Grad-CAM generates a distribution with high values for pixels that contributed more to the network’s decision [49]. In general, with a sufficiently extensive training set, if these techniques show genuine learning, one may infer the model’s adequacy for unseen samples.

### III. RESULTS AND DISCUSSION

#### A. Evaluation of bearing fault diagnosis

Table I illustrates the testing performance of the TF-CNN model and compares it to the two competing methods (T-CNN [4] and PIResNet [47]) across different SNR levels. The results reveal a consistent superiority of the proposed model over the other techniques across all metrics and SNR levels. Additionally, they show that the boost in performance becomes more pronounced when the level of noise increases in the vibration signal. For instance, when utilizing clean data, the TF-CNN outruns PIResNet and T-CNN with 2.2% and 1.6% point gains in accuracy, respectively. Nonetheless, these gains increase to approximately 19% and 15% when dealing with severely degraded vibration signals at -5 dB. This anticipated improvement in performance can be attributed to the uniform distribution of noise within the TF lattice. Consequently, quadratic TFRs are well-suited to unveil distinctive patterns associated with the different bearing faults while concurrently mitigating the influence of noise.

Moreover, the TF-CNN’s confusion matrices are presented in Fig. 5 and suggest that: (1) the *Inner* fault state is the simplest to predict as it has the least drop in successful predictions; from 21,000 for clean signals to 20,776 for

TABLE I  
THE MACRO-AVERAGED TESTING PERFORMANCE. THE RESULTS ARE 5-FOLD AVERAGED ( $\pm$  STANDARD DEVIATIONS), AND THE BEST OUTCOMES ARE IN BOLD. THE PIRESNET RESULTS ARE DRAWN FROM THE REPORTED SINGLE-TRIAL BEST-PERFORMING CONFUSION MATRICES IN [47]; HENCE, SOME STANDARD DEVIATIONS ARE MISSING.

Model	SNR	Accuracy	Precision	Recall	F1-Score
PIResNet [47]	Clean	97.78 $\pm$ 0.18	98.0 $\pm$ N/A	98.0 $\pm$ N/A	98.0 $\pm$ N/A
T-CNN [4]	Clean	98.4 $\pm$ 0.3	98.4 $\pm$ 0.3	98.4 $\pm$ 0.3	98.4 $\pm$ 0.3
TF-CNN	Clean	<b>99.99 <math>\pm</math> 0.01</b>	<b>99.99 <math>\pm</math> 0.01</b>	<b>99.99 <math>\pm</math> 0.01</b>	<b>99.99 <math>\pm</math> 0.01</b>
PIResNet [47]	5 dB	90.26 $\pm$ 0.18	90.5 $\pm$ N/A	90.5 $\pm$ N/A	90.5 $\pm$ N/A
T-CNN [4]	5 dB	91.2 $\pm$ 0.3	91.3 $\pm$ 0.4	91.2 $\pm$ 0.4	91.2 $\pm$ 0.4
TF-CNN	5 dB	<b>99.57 <math>\pm</math> 0.05</b>	<b>99.57 <math>\pm</math> 0.05</b>	<b>99.57 <math>\pm</math> 0.05</b>	<b>99.57 <math>\pm</math> 0.05</b>
PIResNet [47]	0 dB	81.28 $\pm$ 0.36	81.6 $\pm$ N/A	81.6 $\pm$ N/A	81.6 $\pm$ N/A
T-CNN [4]	0 dB	84.0 $\pm$ 0.3	84.0 $\pm$ 0.2	84.0 $\pm$ 0.3	84.0 $\pm$ 0.3
TF-CNN	0 dB	<b>97.55 <math>\pm</math> 0.12</b>	<b>97.55 <math>\pm</math> 0.12</b>	<b>97.55 <math>\pm</math> 0.12</b>	<b>97.55 <math>\pm</math> 0.12</b>
PIResNet [47]	-5 dB	71.67 $\pm$ 0.20	72.3 $\pm$ N/A	72.0 $\pm$ N/A	72.2 $\pm$ N/A
T-CNN [4]	-5 dB	75.3 $\pm$ 0.5	75.1 $\pm$ 0.7	75.3 $\pm$ 0.6	75.2 $\pm$ 0.7
TF-CNN	-5 dB	<b>90.55 <math>\pm</math> 0.16</b>	<b>90.51 <math>\pm</math> 0.17</b>	<b>90.55 <math>\pm</math> 0.17</b>	<b>90.52 <math>\pm</math> 0.17</b>

noisy signals at -5 dB; (2) the *Normal* and *Outer* classes interlace at -5 dB because heavy noise masks their distinct TF signatures; (3) a mild misclassification exists at -5 dB among the *Normal* and *Ball* classes; and (4) by analyzing the confusion matrices’ progression through the increasing levels of noise, there is a slight performance imbalance among the classes at -5 dB. Specifically, the *Normal* and *Outer* states have less successful predictions when compared to the other classes. This observation suggests that intricate TF details are required to distinguish these two states.

#### B. The t-SNE and Grad-CAM analysis

A two-dimensional representation of the TF-CNN learned features is illustrated in Fig. 6 using t-SNE. The results validate the model’s ability to learn state-relevant features in case of clean or noisy vibration data. Specifically, Figs. 6a and 6b show clear inter-class separation among all classes while Fig. 6c depicts a slight overlap between the *Normal* and *Outer* classes. Nonetheless, this overlap escalates when heavy noise is introduced as shown in Fig. 6d. Moreover, the t-SNE results reveal that the *Normal* and *Outer* states are the most alike when degraded with heavy noise, while the *Inner* and *Ball* classes are the most distinct from the rest. These

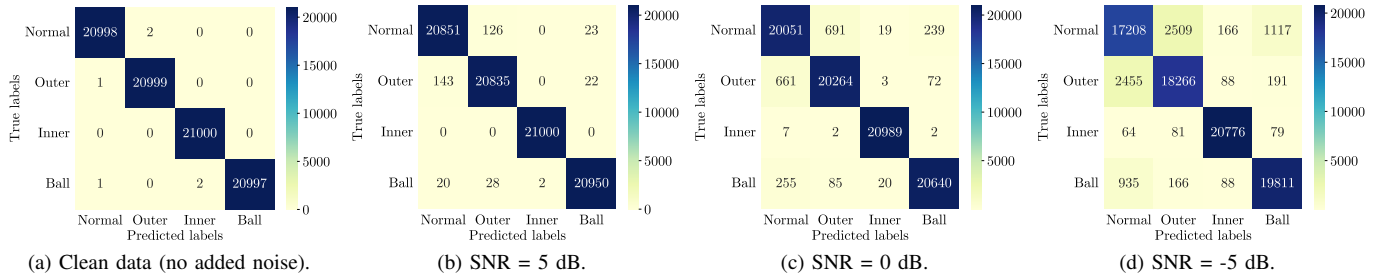


Fig. 5. The testing confusion matrices from all folds when dealing with (a) clean, and (b)-(d) noisy vibration signals.

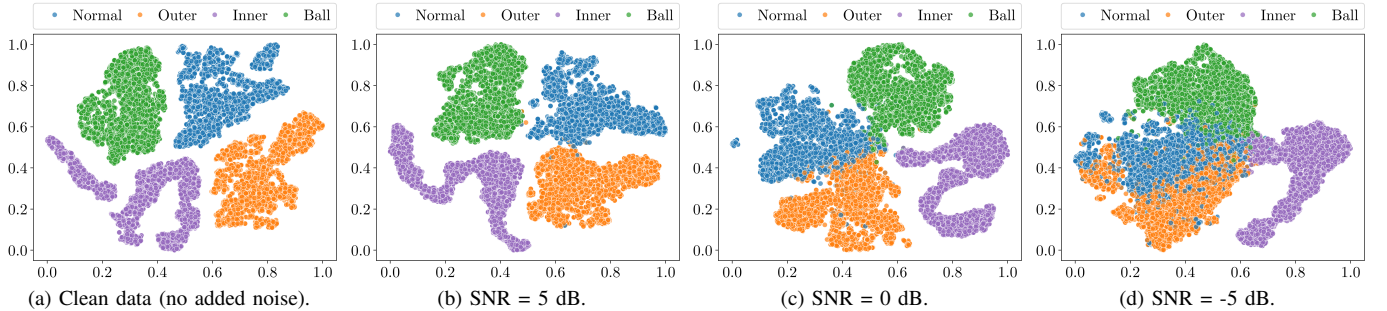


Fig. 6. The t-SNE analysis of the first testing set, using the model's last layer features, when processing (a) clean, and (b)-(d) noisy signals.

observations are aligned with the findings in Fig. 5 and justify the slight performance imbalance at -5 dB. We hypothesize that this alikeness is linked to the characteristic frequency of outer race faults being the lowest among the faults observed. This particular frequency characteristic causes their harmonics to sway less from the resonance of the bearing. Consequently, in the TF domain, outer race faults tend to overlap more with the normal state, and substantial noise can significantly obscure their distinguishing marks.

Furthermore, Fig. 7 illustrates the Grad-CAM outcomes for all the classes along with the rotational speeds for the first 8 seconds of clean vibrations. The visualizations validate our claim that the diagnosis of bearing faults is beyond the scope of basic harmonic analysis. In particular, they underscore the necessity for dynamic features derived from the joint TF domain and indicate apparent limitations when using time-only or frequency-only representations. Additionally, the results showcase the versatility of the proposed model in acquiring fault-relevant non-stationary features, i.e., important descriptors are extracted from regions that evolve in time and frequency; see Figs. 7b-7d. Finally, by associating the rotational speed profiles with the highlighted TF regions, one notes a moderate correspondence between the region's frequency support and the motor's speed, i.e., the regions are temporally coupled with the rotational speeds. However, the outcomes also demonstrate a need for improving the proposed model's attention to generate predictions with higher correlations to the operating variable speeds.

### C. The misclassifications link to speed

The connection between the TF-CNN false decisions at 0 dB SNR and the motor rotational speed is explored in Fig. 8.

First, the temporal locality of the model's misclassifications is presented in Fig. 8a for all the classes. The locale is overlaid on the rotational speed profile for the entire 35 minutes of data, i.e., all the testing data from all the folds. Moreover, Fig. 8b shows the motor speed probability distribution given false predictions and compares it to the speed's unconditional distribution (baseline) for all the bearing health states. Interestingly, the results reveal that misclassifications are most likely to occur at speeds below 1,200 RPM (the lower 1/3 of the entire speed range) where 70%, 100%, 69%, and 73% of all misclassifications exist for the *Normal*, *Inner*, *Outer*, and *Ball* classes, respectively. Additionally, the conditional distributions show that the median speed for which the TF-CNN fails to predict the bearing health state correctly is 1,046 for *Normal*, 840 for *Inner*, 974 for *Outer*, and 992 for the *Ball* state.

The observed skewness towards low speeds can be attributed to the spectral signature of fault-induced vibrations being very close to the bearing's resonance. In other words, the frequency of fault-induced harmonics varies less at those speeds; hence, their TFRs are more likely to be misidentified. Moreover, the constructive accumulation of fault-induced impulses, as described in Eq. (4), is linearly dependent on the rotational speed, i.e., the envelope of the fault signal co-varies with the speed; see Fig. 2b for illustration. Consequently, the ubiquity of the fault signal becomes obscure at severe noise conditions and low operational speeds. These conjectures are aligned with the t-SNE analysis in Fig. 6 and anticipate an increase in the fault-conditioned median speed at lower SNR levels. We verified this prediction at -5 dB SNR and found that the median speed is 1,252 for *Normal* (20% increase), 900 for *Inner* (7% increase), 1,314 for *Outer* (35% increase), and 1,244 for the *Ball* state (25% increase).

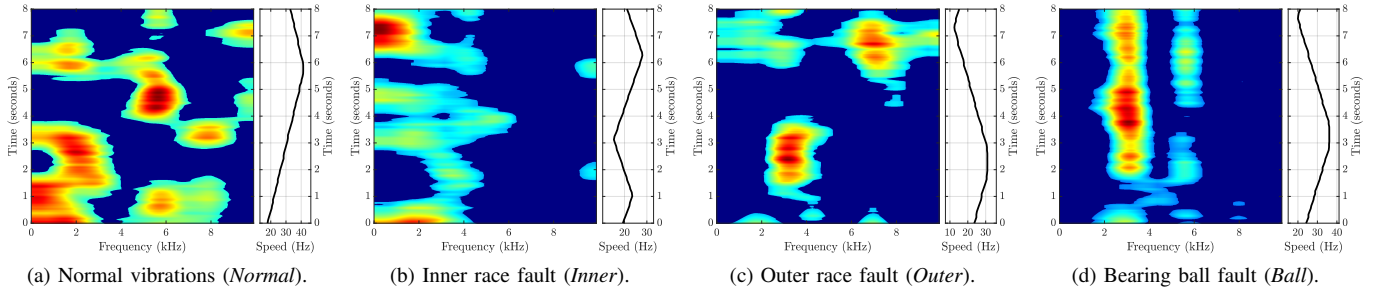
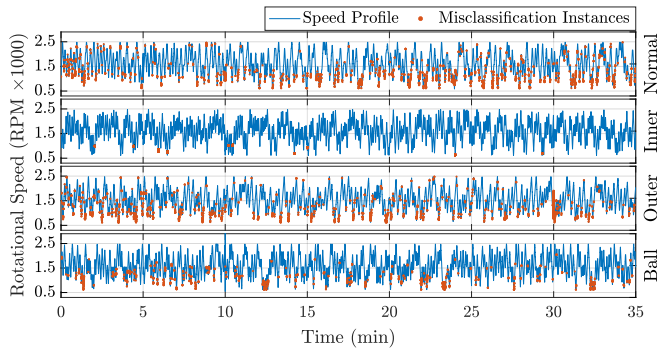
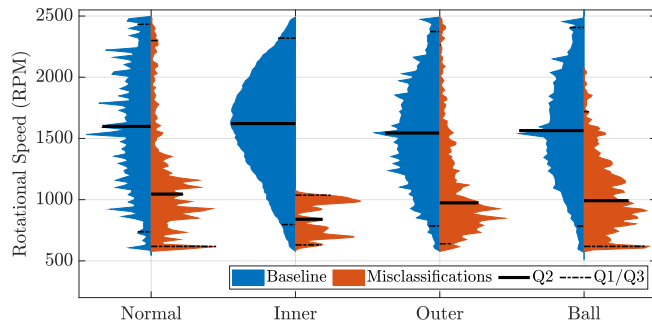


Fig. 7. The Grad-CAM maps and rotational speeds for the first 8 seconds of clean data. The results are formed as follows: (1) generate the Grad-CAM distributions for every segment (0.1 seconds of data); (2) concatenate the results of the first 80 segments in the temporal direction (8 seconds of data); (3) smooth the concatenated results with a 1-second moving average filter; and (4) threshold the smoothed distributions to show their 68.3% confidence interval.



(a) The misclassification temporal locale w.r.t. speed.



(b) The probability distribution of rotational speeds given misclassification.

Fig. 8. The link between misclassification, at 0 dB SNR, and rotational speed for the different bearing health states. (a) shows the temporal locale of misclassifications in relation to the motor’s speed profile, and (b) compares the speed conditional probability distributions given false decisions to the baseline, i.e., the unconditional probability distribution of the time-varying speed. The baseline speed profiles in (a) are interpolated by the modified Akima cubic Hermite interpolation method to match the decisions’ sampling time. The probability distributions in (b) are smoothed using normal kernels and plotted along with their 25% (Q1), 50% (Q2), and 75% (Q3) percentiles.

#### IV. CONCLUSIONS

Bearing faults are major irregularities in rotating machines and they are the main cause of vibration. Analyzing the vibration’s morphology can provide indicators to determine the bearing’s health state. However, current fault diagnosis techniques are designed to operate in highly constrained environments and neglect real-life conditions, e.g., time-varying speeds and the vibration’s non-stationary nature. This study presented a fusion between time-frequency analysis and deep learning techniques to diagnose bearing faults under highly

time-varying rotational speeds and multiple noise levels. First, we modeled the bearing fault-induced vibrations in a general manner and discussed their dynamic spectral evolution. We justified the vibration’s non-stationary behavior and elucidated its association with the bearing’s inherent properties, including its operational parameters such as rotational speed. Moreover, we discussed time-frequency analysis using high-performing quadratic distributions and showed their effectiveness in resolving the vibration waveforms of faulty bearings in comparison to conventional tools, e.g., the Wigner-Ville distribution and the Spectrogram. After that, we designed a CNN network based on the time-frequency compact kernel distribution to diagnose various faults in rolling-element bearings. The experimental results demonstrated the superiority of our method over recently developed techniques. For instance, they showed that quadratic time-frequency distributions are well-suited to unveil distinctive dynamic patterns associated with the different bearing faults while concurrently mitigating the influence of noise. Additionally, they emphasized the versatility of the proposed model in acquiring fault-relevant non-stationary features that are temporally coupled with the rotational speed. In brief, the proposed solution has achieved a remarkable robustness to noise and significant gains in accuracy reaching up to 15% in severe noise conditions.

Our future research directions include testing for other faults, incorporating attention mechanisms, employing post-processing methods, and fusing time-frequency tools with more advanced deep learning techniques such as Operational Neural Networks [50], [51].

#### REFERENCES

- [1] O. AlShorman, M. Irfan, N. Saad, D. Zhen, N. Haider, A. Glowacz, and A. AlShorman, “A Review of Artificial Intelligence Methods for Condition Monitoring and Fault Diagnosis of Rolling Element Bearings for Induction Motor,” *Shock and Vibration*, vol. 2020, p. 8843759, 2020.
- [2] A. Rai and S. H. Upadhyay, “A review on signal processing techniques utilized in the fault diagnosis of rolling element bearings,” *Tribology International*, vol. 96, pp. 289–306, 2016.
- [3] K. C. Deekshith Kompella, M. Venu Gopala Rao, and R. Srinivasa Rao, “Bearing fault detection in a 3 phase induction motor using stator current frequency spectral subtraction with various wavelet decomposition techniques,” *Ain Shams Engineering Journal*, vol. 9, no. 4, pp. 2427–2439, 2018.
- [4] T. Jalonen, M. Al-Sa’d, S. Kiranyaz, and M. Gabbouj, “Real-Time Vibration-Based Bearing Fault Diagnosis Under Time-Varying Speed Conditions,” *arXiv*, 2023.

- [5] T. Ince, J. Malik, O. C. Devecioglu, S. Kiranyaz, O. Avci, L. Eren, and M. Gabbouj, "Early Bearing Fault Diagnosis of Rotating Machinery by 1D Self-Organized Operational Neural Networks," *IEEE Access*, vol. 9, pp. 139 260–139 270, 2021.
- [6] A. Youcef Khodja, N. Guersi, M. N. Saadi, and N. Boutaseta, "Rolling element bearing fault diagnosis for rotating machinery using vibration spectrum imaging and convolutional neural networks," *The International Journal of Advanced Manufacturing Technology*, vol. 106, pp. 1737–1751, 2020.
- [7] C. Malla and I. Panigrahi, "Review of Condition Monitoring of Rolling Element Bearing Using Vibration Analysis and Other Techniques," *Journal of Vibration Engineering & Technologies*, vol. 7, no. 4, pp. 407–414, 2019.
- [8] T. Ince, S. Kiranyaz, L. Eren, M. Askar, and M. Gabbouj, "Real-Time Motor Fault Detection by 1-D Convolutional Neural Networks," *IEEE Transactions on Industrial Electronics*, vol. 63, no. 11, pp. 7067–7075, 2016.
- [9] L. Eren, T. Ince, and S. Kiranyaz, "A Generic Intelligent Bearing Fault Diagnosis System Using Compact Adaptive 1D CNN Classifier," *Journal of Signal Processing Systems*, vol. 91, no. 2, pp. 179–189, 2019.
- [10] O. Abdeljaber, S. Sassi, O. Avci, S. Kiranyaz, A. A. Ibrahim, and M. Gabbouj, "Fault Detection and Severity Identification of Ball Bearings by Online Condition Monitoring," *IEEE Transactions on Industrial Electronics*, vol. 66, no. 10, pp. 8136–8147, 2019.
- [11] T. Jalonen, M. Al-Sa'd, R. Mellanen, S. Kiranyaz, and M. Gabbouj, "Real-Time Damage Detection in Fiber Lifting Ropes Using Convolutional Neural Networks," *arXiv*, 2023.
- [12] Z. Jiang, K. Zhang, L. Xiang, G. Yu, and Y. Xu, "A time-frequency spectral amplitude modulation method and its applications in rolling bearing fault diagnosis," *Mechanical Systems and Signal Processing*, vol. 185, p. 109832, 2023.
- [13] A. Prudhom, J. Antonino-Daviu, H. Razik, and V. Climente-Alarcon, "Time-frequency vibration analysis for the detection of motor damages caused by bearing currents," *Mechanical Systems and Signal Processing*, vol. 84, pp. 747–762, 2017.
- [14] X. Zhang, Z. Liu, J. Wang, and J. Wang, "Time-frequency analysis for bearing fault diagnosis using multiple Q-factor Gabor wavelets," *ISA Transactions*, vol. 87, pp. 225–234, 2019.
- [15] I. Attoui, N. Fergani, N. Boutaseta, B. Oudjani, and A. Deliou, "A new time-frequency method for identification and classification of ball bearing faults," *Journal of Sound and Vibration*, vol. 397, pp. 241–265, 2017.
- [16] G. Tang, Y. Wang, Y. Huang, and H. Wang, "Multiple Time-Frequency Curve Classification for Tacho-Less and Resampling-Less Compound Bearing Fault Detection Under Time-Varying Speed Conditions," *IEEE Sensors Journal*, vol. 21, no. 4, pp. 5091–5101, 2021.
- [17] Z. Feng, M. Liang, and F. Chu, "Recent advances in time-frequency analysis methods for machinery fault diagnosis: A review with application examples," *Mechanical Systems and Signal Processing*, vol. 38, no. 1, pp. 165–205, 2013, condition monitoring of machines in non-stationary operations.
- [18] B. Boashash, Ed., *Time-Frequency Signal Analysis and Processing*, 2nd ed. Oxford: Academic Press, 2016.
- [19] D. Zhang and Z. Feng, "Enhancement of time-frequency post-processing readability for nonstationary signal analysis of rotating machinery: Principle and validation," *Mechanical Systems and Signal Processing*, vol. 163, p. 108145, 2022.
- [20] S. Rajagopalan, J. A. Restrepo, J. M. Aller, T. G. Habetler, and R. G. Harley, "Nonstationary Motor Fault Detection Using Recent Quadratic Time-Frequency Representations," *IEEE Transactions on Industry Applications*, vol. 44, no. 3, pp. 735–744, 2008.
- [21] M. Al-Sa'd, "Time-Frequency Analysis: Application to Electroencephalogram Signal Processing," Ph.D. dissertation, Tampere University, 2022. [Online]. Available: <https://urn.fi/URN:ISBN:978-952-03-2503-9>
- [22] F. Auger, P. Flandrin, Y.-T. Lin, S. McLaughlin, S. Meignen, T. Oberlin, and H.-T. Wu, "Time-Frequency Reassignment and Synchrosqueezing: An Overview," *IEEE Signal Processing Magazine*, vol. 30, no. 6, pp. 32–41, 2013.
- [23] M. Al-Sa'd, B. Boashash, and M. Gabbouj, "Design of an Optimal Piece-Wise Spline Wigner-Ville Distribution for TFD Performance Evaluation and Comparison," *IEEE Transactions on Signal Processing*, vol. 69, pp. 3963–3976, 2021.
- [24] H. Dong, G. Yu, and Q. Jiang, "Time-Frequency-Multisqueezing Transform," *IEEE Transactions on Industrial Electronics*, vol. 71, no. 4, pp. 4151–4161, 2024.
- [25] J. Cai and Y. Xiao, "Time-frequency analysis method of bearing fault diagnosis based on the generalized S transformation," *Journal of Vibro-engineering*, vol. 19, no. 6, pp. 4221–4230, sep 2017.
- [26] L. Wang, J. Xiang, and Y. Liu, "A time-frequency-based maximum correlated kurtosis deconvolution approach for detecting bearing faults under variable speed conditions," *Measurement Science and Technology*, vol. 30, no. 12, p. 125005, sep 2019.
- [27] Y. Zhang, K. Xing, R. Bai, D. Sun, and Z. Meng, "An enhanced convolutional neural network for bearing fault diagnosis based on time-frequency image," *Measurement*, vol. 157, p. 107667, 2020.
- [28] S. Li, W. Yang, A. Zhang, H. Liu, J. Huang, C. Li, and J. Hu, "A Novel Method of Bearing Fault Diagnosis in Time-Frequency Graphs Using InceptionResnet and Deformable Convolution Networks," *IEEE Access*, vol. 8, pp. 92 743–92 753, 2020.
- [29] Y. Kaya, F. Kuncan, and H. Ertunc, "A new automatic bearing fault size diagnosis using time-frequency images of CWT and deep transfer learning methods," *Turkish Journal of Electrical Engineering and Computer Sciences*, vol. 30, no. 5, pp. 1851–1867, 2022.
- [30] Z. Chen, J. Cen, and J. Xiong, "Rolling Bearing Fault Diagnosis Using Time-Frequency Analysis and Deep Transfer Convolutional Neural Network," *IEEE Access*, vol. 8, pp. 150 248–150 261, 2020.
- [31] R. Wang, J. Zhang, H. Fang, L. Yu, and J. Chen, "Sparsity enforced time-frequency decomposition in the Bayesian framework for bearing fault feature extraction under time-varying conditions," *Mechanical Systems and Signal Processing*, vol. 185, p. 109755, 2023.
- [32] G. Yu, "A Concentrated Time-Frequency Analysis Tool for Bearing Fault Diagnosis," *IEEE Transactions on Instrumentation and Measurement*, vol. 69, no. 2, pp. 371–381, 2020.
- [33] I. Quinde, J. Sumba, L. Ochoa, A. J. Guevara, and R. Morales-Menendez, "Bearing Fault Diagnosis Based on Optimal Time-Frequency Representation Method," *IFAC-PapersOnLine*, vol. 52, no. 11, pp. 194–199, 2019, 5th IFAC Conference on Intelligent Control and Automation Sciences ICONS 2019.
- [34] J. Wang, Z. Mo, H. Zhang, and Q. Miao, "A Deep Learning Method for Bearing Fault Diagnosis Based on Time-Frequency Image," *IEEE Access*, vol. 7, pp. 42 373–42 383, 2019.
- [35] G. Dong and J. Chen, "Noise resistant time frequency analysis and application in fault diagnosis of rolling element bearings," *Mechanical Systems and Signal Processing*, vol. 33, pp. 212–236, 2012.
- [36] A. Vitor, A. Goedel, M. F. Castoldi, W. A. Souza, and G. H. Bazan, "Induction Machine Fault Diagnosis With Quadratic Time-Frequency Distributions: State of the Art," *IEEE Transactions on Instrumentation and Measurement*, vol. 72, pp. 1–16, 2023.
- [37] A. Kumar and R. Kumar, "Role of Signal Processing, Modeling and Decision Making in the Diagnosis of Rolling Element Bearing Defect: A Review," *Journal of Nondestructive Evaluation*, vol. 38, no. 1, p. 5, 2018.
- [38] N. Sawalhi and R. B. Randall, "Vibration response of spalled rolling element bearings: Observations, simulations and signal processing techniques to track the spall size," *Mechanical Systems and Signal Processing*, vol. 25, no. 3, pp. 846–870, 2011.
- [39] "Rolling element bearing schematic." [Online]. Available: [https://upload.wikimedia.org/wikipedia/commons/f/f6/HARP\\_bearing.jpg](https://upload.wikimedia.org/wikipedia/commons/f/f6/HARP_bearing.jpg)
- [40] S. Kim, D. An, and J.-H. Choi, "Diagnostics 101: A Tutorial for Fault Diagnostics of Rolling Element Bearing Using Envelope Analysis in MATLAB," *Applied Sciences*, vol. 10, no. 20, 2020.
- [41] Z. Feng, X. Chen, and T. Wang, "Time-varying demodulation analysis for rolling bearing fault diagnosis under variable speed conditions," *Journal of Sound and Vibration*, vol. 400, pp. 71–85, 2017.
- [42] H. Saruhan, S. Saridemir, A. Qicek, and I. Uygur, "Vibration analysis of rolling element bearings defects," *Journal of applied research and technology*, vol. 12, no. 3, pp. 384–395, 2014.
- [43] H. Cheng, Y. Zhang, W. Lu, and Z. Yang, "Research on ball bearing model based on local defects," *SN Applied Sciences*, vol. 1, no. 10, p. 1219, 2019.
- [44] X. Zhang, Q. Han, Z. Peng, and F. Chu, "A new nonlinear dynamic model of the rotor-bearing system considering preload and varying contact angle of the bearing," *Communications in Nonlinear Science and Numerical Simulation*, vol. 22, no. 1, pp. 821–841, 2015.
- [45] B. Boashash, A. A. El-Bey, and M. F. Al-Sa'd, "Multisensor Time-Frequency Signal Processing MATLAB package: An analysis tool for multichannel non-stationary data," *SoftwareX*, vol. 8, pp. 53–58, 2018, digital Signal Processing & SoftwareX - Joint Special Issue on Reproducible Research in Signal Processing.
- [46] W. Jung, S.-H. Kim, S.-H. Yun, J. Bae, and Y.-H. Park, "Vibration, acoustic, temperature, and motor current dataset of rotating machine

under varying operating conditions for fault diagnosis,” *Data in brief*, vol. 48, pp. 109049–109049, 2023.

- [47] Q. Ni, J. C. Ji, B. Halkon, K. Feng, and A. K. Nandi, “Physics-Informed Residual Network (PIResNet) for rolling element bearing fault diagnostics,” *Mechanical Systems and Signal Processing*, vol. 200, p. 110544, 2023.
- [48] L. van der Maaten and G. Hinton, “Visualizing data using t-SNE,” *Journal of Machine Learning Research*, vol. 9, no. 86, pp. 2579–2605, 2008.
- [49] R. R. Selvaraju, M. Cogswell, A. Das, R. Vedantam, D. Parikh, and D. Batra, “Grad-CAM: Visual Explanations From Deep Networks via Gradient-Based Localization,” in *Proceedings of the IEEE International Conference on Computer Vision (ICCV)*, Oct. 2017, pp. 618–626.
- [50] S. Kiranyaz, T. Ince, A. Iosifidis, and M. Gabbouj, “Operational neural networks,” *Neural Computing and Applications*, vol. 32, no. 11, pp. 6645–6668, 2020.
- [51] S. Kiranyaz, J. Malik, H. B. Abdallah, T. Ince, A. Iosifidis, and M. Gabbouj, “Self-organized Operational Neural Networks with Generative Neurons,” *Neural Networks*, vol. 140, pp. 294–308, 2021.



**Serkan Kiranyaz** (Senior Member, IEEE) is a Professor with Qatar University, Doha, Qatar. He published two books, five book chapters, more than 80 journal articles in high impact journals, and 100 articles in international conferences. He made contributions on evolutionary optimization, machine learning, bio-signal analysis, computer vision with applications to recognition, classification, and signal processing. He has coauthored the articles which have nominated or received the “Best Paper Award” in ICIP 2013, ICPR 2014, ICIP 2015, and IEEE Transactions on Signal Processing (TSP) 2018. He had the most-popular articles in the years 2010 and 2016, and most-cited article in 2018 in IEEE Transactions on Biomedical Engineering. From 2010 to 2015, he authored the 4th most-cited article of the Neural Networks journal. His research team has won the second and first places in PhysioNet Grand Challenges 2016 and 2017, among 48 and 75 international teams, respectively. His theoretical contributions to advance the current state of the art in modeling and representation, targeting high long-term impact, while algorithmic, system level design and implementation issues target medium and long-term challenges for the next five to ten years. He in particular aims at investigating scientific questions and inventing cutting-edge solutions in “personalized biomedicine” which is in one of the most dynamic areas where science combines with technology to produce efficient signal and information processing systems.



**Mohammad Al-Sa'd** (Senior Member, IEEE) received his B.Sc. and M.Sc. degrees in Electrical Engineering from Qatar University, Qatar, in 2012 and 2016, respectively, and his PhD degree in Electrical Engineering and Computing Sciences from Tampere University, Finland, in 2022. He specialized in signal processing and he is pursuing his postdoctoral fellowship at the Department of Physiology, University of Helsinki, Finland, and at the Department of Computing Sciences, Tampere University, Finland.

He has served as a technical reviewer for several journals, including IEEE Transactions on Signal Processing, Digital Signal Processing, Signal Processing, Biomedical Signal Processing and Control, and IEEE Access. His research interests include time-frequency signal analysis, machine learning, electroencephalogram analysis and processing, information flow and theory, signal modeling, and optimization.



**Moncef Gabbouj** (Fellow Member, IEEE) received the B.S. degree from Oklahoma State University, Stillwater, OK, USA, in 1985, and the M.S. and Ph.D. degrees from Purdue University, in 1986 and 1989, respectively, all in electrical engineering. He is a Professor of signal processing with the Department of Computing Sciences, Tampere University, Tampere, Finland. He was an Academy of Finland Professor from 2011 to 2015. His research interests include big data analytics, multimedia content-based analysis, indexing and retrieval, artificial intelligence, machine learning, pattern recognition, nonlinear signal and image processing and analysis, voice conversion, and video processing and coding.

Dr. Gabbouj is a member of the Academia Europaea and the Finnish Academy of Science and Letters. He is the past Chairman of the IEEE CAS TC on DSP and the Committee Member of the IEEE Fourier Award for Signal Processing. He served as an Associate Editor and the Guest Editor of many IEEE, and international journals and a Distinguished Lecturer for the IEEE CASS. He is the Finland Site Director of the NSF IUCRC funded Center for Visual and Decision Informatics (CVDI) and leads the Artificial Intelligence Research Task Force of the Ministry of Economic Affairs and Employment funded Research Alliance on Autonomous Systems (RAAS).



**Tuomas Jalonen** received the B.Sc. and M.Sc. degrees in mechanical engineering from Tampere University, Finland, in 2017 and 2019, respectively. He is currently pursuing the Ph.D. degree with the Faculty of Information Technology and Communication Sciences of Tampere University, Finland. His research interest includes the development of machine learning applications for manufacturing.